An experimental and numerical study of plunging wave impact on a box-shape structure

Bin Yan[a], Min Luo[b,*], Wei Bai[c]

[a] College of Civil Engineering, Shenzhen University, 3688 Nanhai Road, Nanshan District, Shenzhen 518060, China
[b] College of Engineering, Swansea University Bay Campus, Swansea, SA1 8EN, UK
[c] School of Computing, Mathematics and Digital Technology, Manchester Metropolitan University, Chester Street, Manchester M1 5GD, UK

Abstract

The plunging wave impacts on a box-shape structure are investigated experimentally and numerically, focusing on three typical scenarios with distinct features, i.e. the wave impact occurs after, upon and before wave breaking. In the experiments, the plunging wave is generated by a piston-type wave maker whose motion is governed by the focused wave theory. The fixed box-shape structure mimics the offshore platform structures. Measured are the wave elevations at typical positions, the wave impact pressures on the front and bottom (violent impact is very likely to occur) of the platform, and the wave profiles of the transient wave impact process. The experiment identifies the pressure maximums both on the front and bottom walls under three different wave impacts. The pressure oscillation along the front wall is observed and analyzed by examining the evolution of air cavity. The experimental parameters and dimensions including the actual wave maker motion signal was inputted into the numerical model to reproduce the same case. Numerical simulations using an improved immersed boundary method are compared with the experimental results with roughly good agreements being achieved. Besides, numerical pressure distributions along the front and bottom walls are presented to find different modes of wave impact. Finally, the maximal pressures on the front wall of the box-shape structure are normalized by two approaches, and compared with the documented maximal pressure ranges.

Keywords: Plunging wave, Pressure oscillation, Wave impact, Box-shape structure, Immersed boundary method

1. Introduction

As the global environment changes, extreme wave events may occur more frequently. With huge destructive power, those extreme waves can cause catastrophic damages to the offshore and coastal structures. The extreme wave impact process is quite complicated and still a challenging topic in the CFD (Computational Fluid Dynamics) community. In some circumstances, the extreme wave entraps some air, which seems to

*Corresponding author
Email address: min.luo@swansea.ac.uk (Min Luo)

significantly affect the local wave impact characteristics (Chan, 1994, Wood Deborah et al., 2000, Bredmose et al., 2010). The highly non-linear water-air interaction makes this problem more complicated.

Extensive researchers have devoted their efforts to investigating the characteristics of wave impact. Blackmore and Hewson (1984) measured the impact pressure on Ilfracombe seawall in the field under broken waves and found that the pressure was lower than those measured in the scaled experiments. The phenomenon is ascribed to the high-percentage of air cavity. To account for the air volume fraction during an air entrapment process well, Blackmore and Hewson (1984) introduced a factor λ in the prediction of pressure p under broken waves with an expression: $p = \lambda \rho C^2 T$, where ρ, C and T are the water density, wave celerity and wave period respectively. As the experiment cannot scale the high percentage of air entrained in the wave by the Froude scaling law, it captured the relatively higher pressure value than the field observation. Thus, the factor in the model test (1$\sim$10) is generally larger λ than that in the field observation (0.1$\sim$0.5). The larger λ means more percentage of air is entrained in the wave, which can cause higher pressure. Chan (1994) examined the pressure on a vertical wall subjected to the plunging wave impact. They concluded that the impact pressure consists of two components: one related to normal wave evolution and the other one determined by the air trapped. In the simulation of plunging wave on a vertical wall in Wood Deborah et al. (2000), the presence of air did not prolong the peak pressure, but enlarged the magnitude of its impulse on the structure.

Bullock et al. (2007) studied the wave impact on vertical and sloping walls experimentally, and found that the characteristics of wave impact are highly dependent on the breaking condition. Particularly, this study classified four different types of wave impact, i.e. slightly-breaking, low aeration, high-aeration and broken wave impact. Considering one type of wave impact, in Bredmose et al. (2010), the experimental and numerical simulations (the potential flow theory) for a flip-through wave impact on a typical seawall were conducted. The results indicated that the impact pressure is extremely sensitive to the shape of impact wave. Cuomo et al. (2010) conducted an experimental study on a vertical wall connected by a slope, who normalized the pressure by $\rho g H_D$ (g is the acceleration of gravity and H_D is the designed wave height). The experimental maximal normalized parameter of $\rho g H_D$ was almost 4.5. Bredmose et al. (2015) continued to investigate the breaking impact on a typical wall and examined the effect of aeration. It found that more aeration reduces the impact pressure and force on the wall.

For a simplification of a front wall of an FPSO (Floating Production Storage and Offloading) hull, modeling a unidirectional breaking wave impacting a rigid wall was conducted in Guilcher et al. (2013) by the SPH (Smoothed Particle Hydrodynamics) method. The results of two different scales were compared with each other. The experiment at the scale 1:6 showed a higher pressure maximum in the aeration area than that at the scale 1:1. This conclusion was also applied to the frequency of pressure oscillations. Smaller scale experiment captured higher pressure value, which agreed with the conclusion in Blackmore and Hewson (1984). With a Consistent Particle Method (CPM), Luo et al. (2016) simulated the dam break in a tank. The pressures on the vertical boundary wall of the tank were recorded, indicating that the pressure oscillation is closely linked with the compression or expansion of air pocket. For a better understanding of mechanics of breaking wave impact, Hu et al. (2017) modeled four types of wave impact (slightly-breaking, flip-through, large air pocket and broken wave impact) on a truncated wall in the numerical and experimental flumes. Among four types of wave impact, the flip-through impact captured the highest pressure value.

In addition to the impact on the vertical wall, there are some papers focusing on the bottom of a structure. Ren et al. (2006) investigated the flow field underneath a thin plate and impact pressure on the bottom wall. The correlation between the impact pressure and water velocity was examined. Gao et al. (2012) studied the regular wave impact on the bottom of a thin plate with an improved SPH method. The velocity and pressure field near the structure were investigated. The pressure field along the bottom surface remained stable under the regular wave condition. Abdussamie et al. (2016) adopted a thick deck (simplification of a tension leg platform) to study the wave impact, but they only focused on the impact event over the bottom wall. The static set-down of the deck had a significant effect on the loads over the bottom surface of deck. Qin et al. (2017) carried out a numerical simulation of nonlinear freak wave impact underneath a fixed horizontal 2D deck. It observed that under the freak wave conditions, large wave impact may happen with a relatively big deck clearance (e.g. the survival draft of deep-sea platforms). It also found a strong effect of deck clearance on the loads over the bottom wall of deck.

Most of the above-mentioned studies investigated the wave impacts on a vertical wall or on the bottom surface of thin plate structures. For the box-shape structures such as the oil/gas platform, the wave impacts on both the top and bottom of the structure are critical factors, which should be comprehensively considered in the design. In this context, this study investigates the typical extreme wave impacts on the bottom and front wall of a fixed box-shape structure, through carefully controlled experiments and numerical simulations, which has been rarely investigated before. The characteristics of the wave impact pressure under different wave impact scenarios with quite small time intervals are focused. More importantly, the oscillation of wave impact pressure on the front wall of the structure is observed and its correlation with the air entrapment is explored, which is so far not well understood. The experimental elevations and pressures are employed to validate the numerical method (immersed boundary method, Yan et al. (2018)). Using the validated numerical method, the impact pressure distributions on the front and bottom walls of the structure are investigated. The peak pressure values are analyzed and found to be located within the range documented by Blackmore and Hewson (1984) and Cuomo et al. (2010).

2. Experimental investigation

2.1. Experimental setup

An experimental study is conducted in the ferrocement wave flume (36 m $\times$ 2 m $\times$ 1.3 m) in the hydraulic laboratory at National University of Singapore. Waves are generated by a piston type wave paddle. The downstream end of the wave flume is a sloping beach that absorbs wave and hence minimizes the wave reflection. The platform structure is a hollow box of 0.12 m height and of 0.5 m length (along the wave flume direction), made of perspex of 10 mm thickness. The platform is of width 1.95 m and installed in the middle of the wave flume. Hence there is a 2.5 cm gap at each side of the platform from the flume wall (for ease of structure installation). The ratio of the gap distance to the flume width is 1.25 %. Such a small gap has a limited influence on the wave motion. In addition, the influences exist mainly near the flume wall. Therefore, the wave motion near the flume center can be reasonably assumed to be two-dimensional (2D). Considering that all the measurements of wave elevations and pressures are on the center line of the wave flume, the gaps at both sides and the water entered do not produce significant nonlinear forces that differ from a perfect 2D case. Stiffeners are added in the platform to stiffen the walls of the platform, ensuring that the platform performs as a rigid body. The platform is fixed by a vertical support plate, which is supported by a steel frame from the downstream side. The maximum lateral deflection of the platform was around 2 mm, being very small compared to the structure dimension. In addition, the frequency of the structural lateral deflection (around 1 Hz) is more than one order of magnitude away from those of the pressure responses on the platform (the values can be seen from Figs. 5 and 7). Therefore, the effect of the tiny structural deflection on the pressure and force responses on the structure is negligible. The bottom of the platform is 0.749 m from the flume bottom, 0.049 m above the mean water level. The front wall of the platform is 13.771 m from the initial position of the wave paddle (see Fig. 1(a)). Four ATM.1ST analogy gauge pressure sensors of measurement range 0.1 bar (accuracy is 0.1 % full scale and response time is less than 1 millisecond) are installed on the upstream part of the platform to measure the extreme wave impact pressures at typical positions. Their positions are shown in Fig. 1(b) and Fig. 1(d): FP1 and FP2 at the front, and BP1 and BP2 at the bottom. To measure the wave elevations, three wave gauges are installed at 6.694 m, 9.459 m and 10.904 m respectively from the wave paddle on the center line of the wave flume. A high-speed camera is placed perpendicular to the glass wall of the wave flume, near the platform, to capture the transient wave motion.

2.2. Plunging wave generation

The plunging wave is generated using the focused wave theory. The basic idea is that a group of linear waves with different frequencies propagate at different velocities and their crests occur simultaneously at a specified point in space and time, producing a large amplitude wave, which will develop into a plunging breaker subsequently. By superposition of all wave components, the wave elevations with space x and time t is as follows (Ma et al., 2009; Zhao and Hu, 2012),

$$\eta(x,t) = \sum_{i=1}^{N} a_i cos\left[k_i(x_i - x_f) - 2\pi f_i(t - t_f)\right]. \tag{1}$$

The meanings of those variables in Eq. 1 are presented in Table 1. The theoretical amplitude of the focused wave at the focusing position is the summation of a_i (0.197 m for the three wave cases), but the actual wave amplitude is smaller than this value because of wave nonlinearity. Three wave impact scenarios are studied, i.e. wave impacts on the platform before, upon and after wave breaking, by changing x_f in Eq. 1

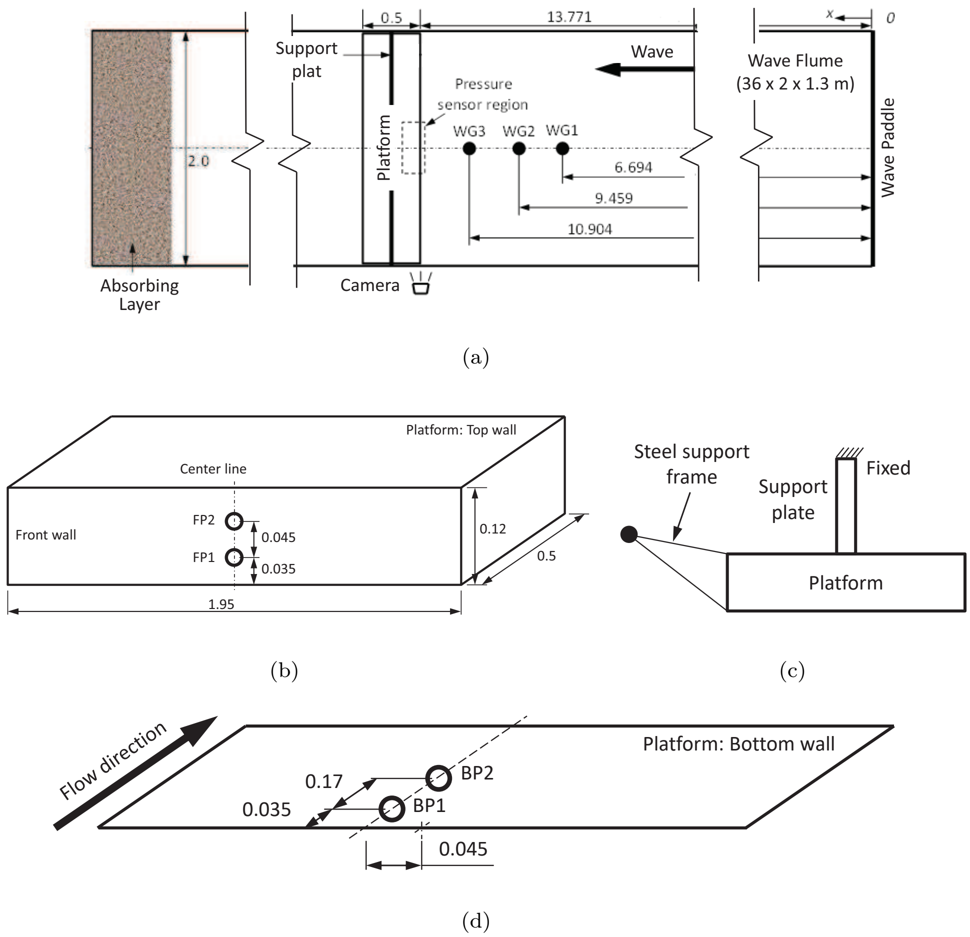

Figure 1: Schematic view and dimension of the experimental setup (unit: m): (a) plan view; (b) platform and sensor hole positions; (c) section view of the platform; (d) bottom wall of the platform.

Table 1: Plunging wave parameters

Water depth	d	0.7m
Number of wave components	N	32
Frequency band	$[f_{min}, f_{max}]$	[0.32Hz, 0.96Hz]
Amplitude of the i-th component	a_i	0.0061m (Chan, 1994)
Frequency of the i-th component	f_i	Uniformly selected in the frequency band
Wave number of the i-th component	k_i	Computed by dispersion equation
Characteristics wave frequency	$f = (f_{min} + f_{max})/2$	0.64Hz
Characteristics wave length	L	3.312m
Characteristics wave celerity	C	2.11m/s
Focusing position / time	x_f / t_f	12.4m / 20.832s (Impact after breaking, S1) 12.45m / 20.857s (Impact upon breaking, S2) 12.8m / 20.902s (Impact before breaking, S3)

(and hence the wave breaking location) so as to investigate the characteristics of wave impact on a structure with the wave forms before the impact occurs. Once the target wave is specified, a transfer function (Biesel and Suquet, 1951) is used to compute the wave paddle motion. The focusing time t_f is determined in such a way that the paddle motion is zero when $t = 0$. In the experiments, the actual wave paddle displacements are measured by a linear variable differential transformer (LVDT). As shown in Fig. 2, the measured paddle motion matches well with the theoretical paddle motion. It shows the precision of the paddle control system. Based on measured paddle motion, the wave paddle velocities are computed and used as the excitation input in the numerical simulations.

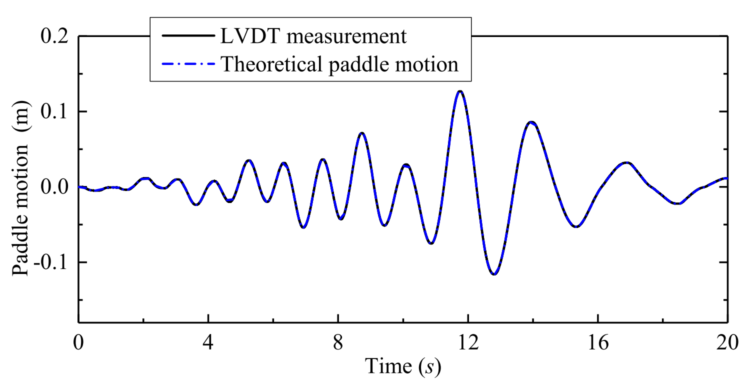

Figure 2: Wave paddle motion: control system input VS. LVDT of S2 measurement.

Three wave packets are generated and the associated parameters are presented in Table 1. Those three wave packets have the same wave frequency and amplitude components. The difference between them is the focal position (and hence focal time). Particularly, in S1 the wave packet focuses at a nearest position from the wave paddle. Wave packets S2 and S3 focus at a middle and furthest position, respectively. The focal positions of three cases are designed such that the wave breaks already (S1), just breaks (S2) and does not break yet (S3) in the wave interaction with the structure. This allows an investigation on how the wave profile (upon wave impact occurs) affects the dynamic wave impact process, by keeping the same wave energy input (Hu et al., 2017).

2.3. Experimental results

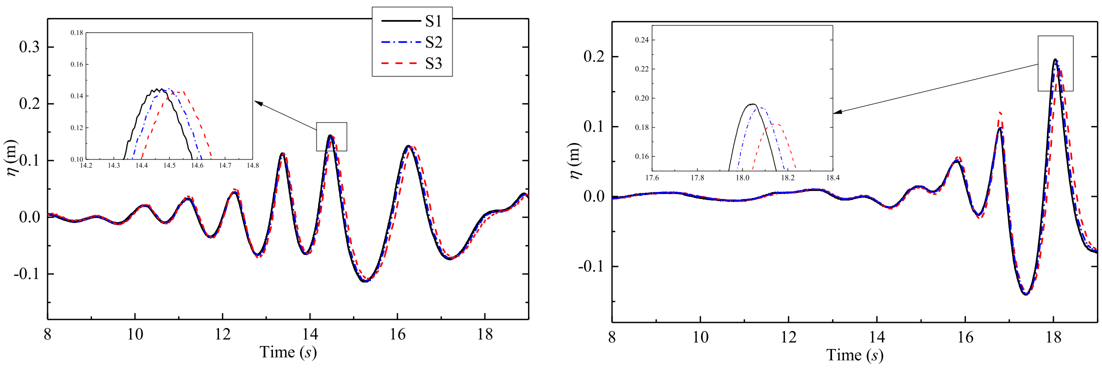

(a) (b)

Figure 3: Experimental wave elevations with different inputted signals (S1, S2, S3): (a) WG1; (b) WG3.

As shown in Fig. 3, the time histories of wave elevation at WG1 and WG3 of three cases are presented. Due to the wave focusing, a large wave appears at WG3 with the amplitude of almost 0.197 m. The subtle difference between the three cases is the phase lag revealed in Table 1 and the magnitude of wave height. The waves of S1 and S2 possess a similar wave height while the wave of S3 has a smaller wave height compared to those of S1 and S2. The maximal wave height occurs in S1, shown in Fig. 3(b), is about 0.34 m, resulting in a very high wave steepness (about 0.1). The larger wave steepness easily leads to wave breaking.

Fig. 4 gives the snapshots of wave profile during the transiting period when the wave approaches and interacts with the platform. The wave of S2 breaks as soon as it impacts the deck, while the wave of S3 is non-breaking when it reaches the front wall of the deck. For the wave of S1, it impacts the front wall of the deck after breaking. The waves of S1 and S2 show the breaking features, whereas the wave of S3 is still developing in front of the deck. In addition, the waves of S1 and S2 entrap more air than that of S3. The air entrapment has a significant influence on the impact pressure, which will be discussed later. Based on those features and the categorization from Hu et al. (2017), these three wave impacts can be classified as the corresponding types. The impacts of S1 and S2 correspond to large air pocket impact while the impact of S3 belongs to slightly-breaking impact.

Fig. 5 shows the time histories of pressure at four stations under three wave conditions. For the pressure at BP1, three waves lead to the similar magnitude of impact pressure about 4.0 kpa. More details about

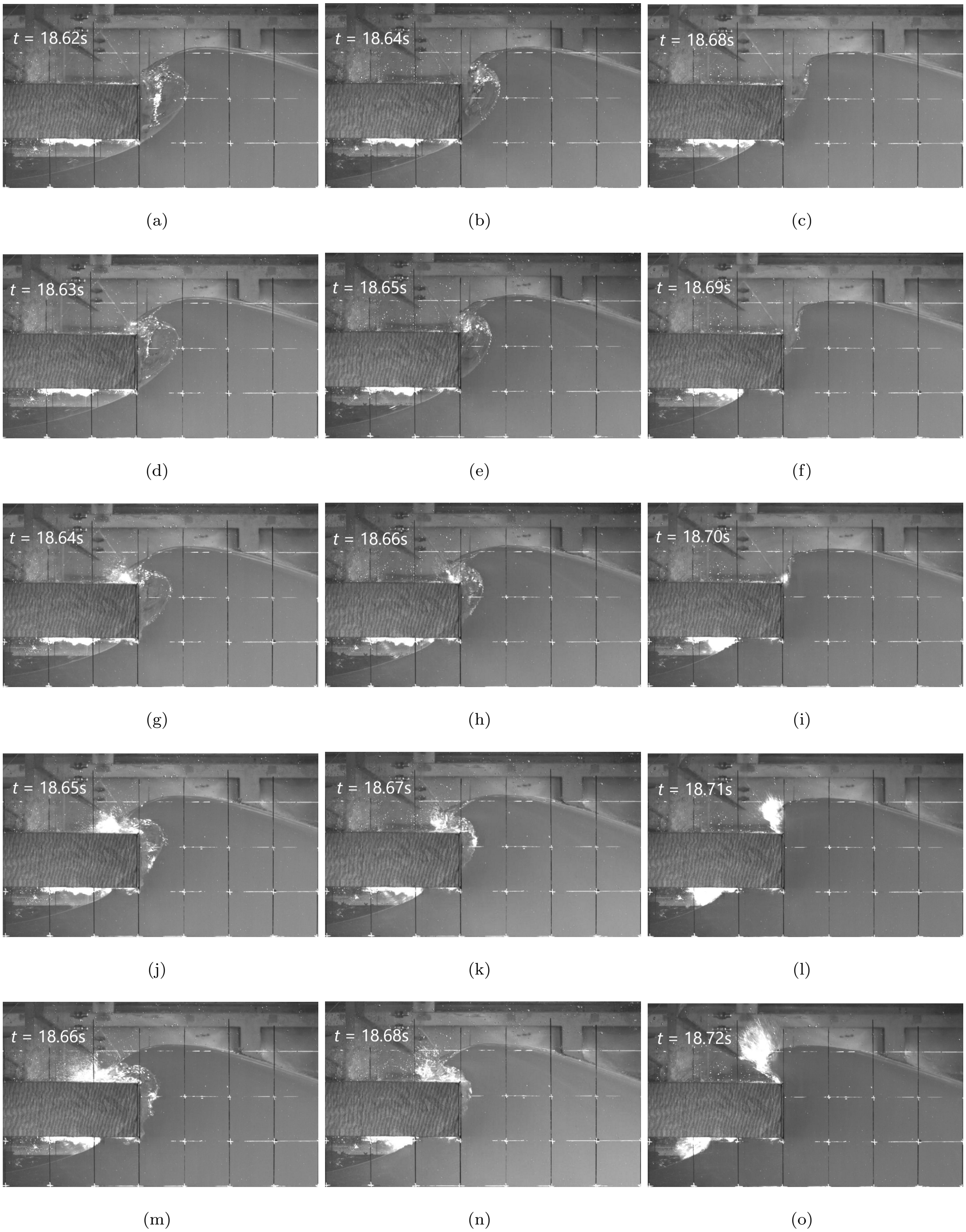

Figure 4: Snapshots of the wave impact process for the three wave scenarios. Left column: S1; middle column: S2; right column: S3.

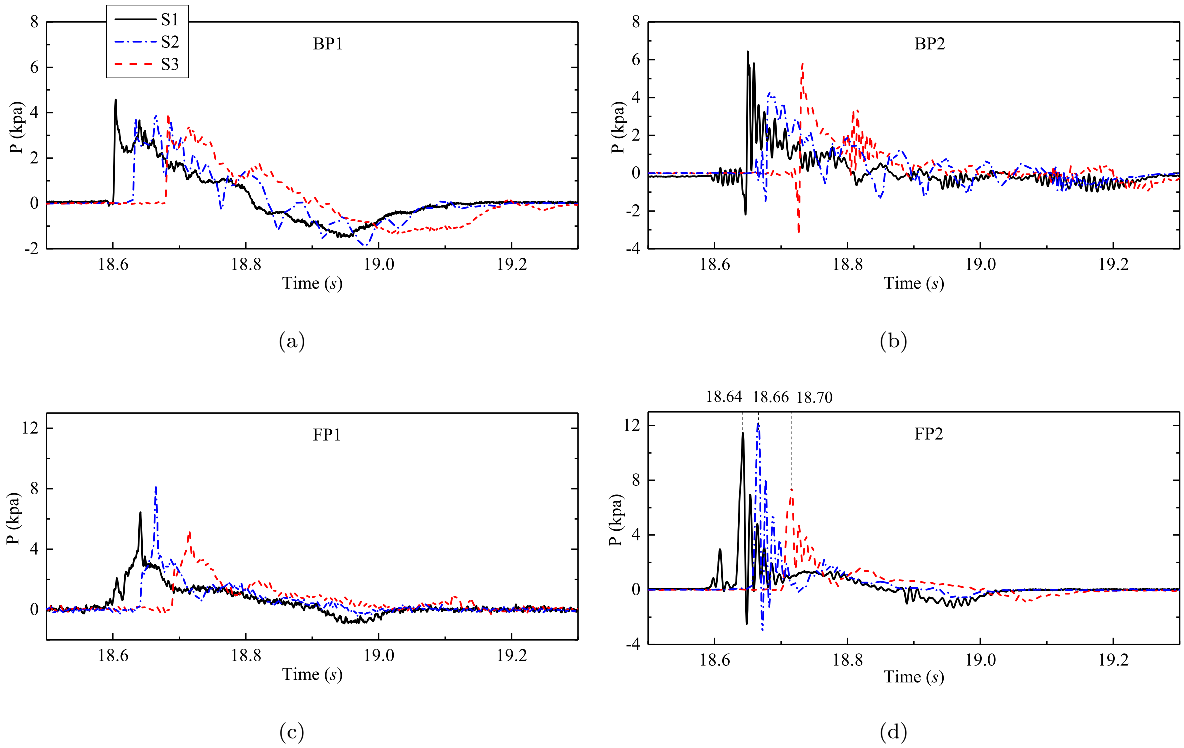

Figure 5: Comparison of pressure among three types of plunging waves (S1, S2, S3) at various positions: (a) BP1; (b) BP2; (c) FP1; (d) FP2.

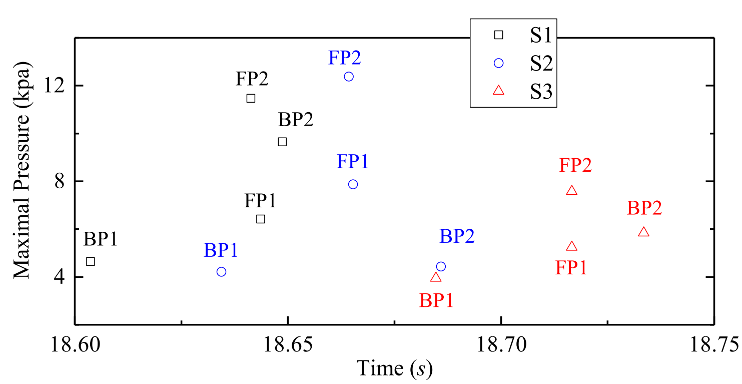

Figure 6: Occurrence of maximal pressure among three types of plunging waves.

Table 2: Maximal positive and negative pressures in the three cases.

Stations	Maximal positive pressure /kpa			Maximal negative pressure /kpa		
	S1	S2	S3	S1	S2	S3
BP1	4.648	3.946	3.846	-1.468	-1.836	-1.368
BP2	6.501	4.332	5.933	-2.178	-1.551	-3.067
FP1	6.475	8.184	5.126	-0.957	-0.399	-0.236
FP2	11.475	12.162	7.532	-2.493	-3.204	-1.015

the maximal positive and negative pressures are listed in Table 2. In addition to the impact pressure, this station is also subjected to suction pressure (negative), which is about 2.0 kpa in three situations. Secondly, Fig. 5(b) shows the pressure at another station on the bottom surface, which is farther downstream than BP1. As BP2 is closer to the water front underneath the deck in the wave propagation, the interaction between the wave front and bottom wall of deck is stronger. Thus, BP2 captures a larger peak pressure value than BP1. At BP2, the suction pressure approaches 3.0 kpa, but with the shorter time duration than that at BP1. In addition, an evident pressure oscillation around $t = 18.8$ s is observed when the wave impacts the bottom wall in S3. It may be caused by the entrained air around the bottom wall, which is easy to be formed in S3 (see Fig. 4(o)). The mechanism is similar to the pressure oscillation on the front wall of the platform (see the FP2 result in Fig. 5). The phenomenon was also pointed out by Faltinsen et al. (2004) and Lind et al. (2015).

The pressures on the front wall are presented in Fig. 5(c) and Fig. 5(d), where the higher maximal pressure values than those along the bottom surface are observed and approaching 12.0 kpa. The magnitude at FP1 is slightly smaller than that at FP2. As the position of FP1 is lower than FP2, FP1 is easily submerged by the water in the wave impact process and affected less by the air cavity than FP2. Thus, the station FP1 captures a smaller peak pressure. Compared with Fig. 5(c), there exists the larger negative pressure in Fig. 5(d). Both the negative pressures at BP2 and FP2 are higher than those at BP1 and FP1. It may be caused by the more air entrained around the positions BP2 and FP2 (see Fig. 4), which easily leads to the pressure oscillation. The pressure oscillation may be induced by the escape or inflation of air cavity around the bottom and front walls. The phenomenon was also pointed out by Chan and Melville (1988) and Hu et al. (2017).

The peak pressures and their time instants of occurrence of the three cases are plotted in Fig. 6. In all three cases, the maximal pressure occurs at FP2. The maximal pressure at BP1 appears earlier than those at FP1 and FP2, while the pressure at BP2 approaches its maximum later than those at FP1 and FP2. The station FP1 contacts the water earliest and the wave impact on the front wall occurs successively after that at FP1. And BP2 is farther than BP1 and the front wall. Thus, the wave impact at BP2 occurs at last.

2.4. Pressure Oscillation

The last subsection shows the pressure oscillation observed at FP2 for the waves of S1 and S2. More details are reflected in Fig.7, where the pressure oscillation is zoomed in. The pressure time history reveals a stable oscillation period $T = 0.011$ s for both the waves of S1 and S2. Both Topliss et al. (1993) and Abrahamsen and Faltinsen (2012) derived the formula of the natural frequency for the air pocket on a vertical wall, in which the shape of air pocket was assumed to be a semi-circle. Abrahamsen and Faltinsen (2012) also claimed that the frequency is related to the shape of air cavity and water surface outside the air cavity. Lugni et al. (2010) threw a deep insight into the mechanism of the pressure oscillation.

According to Lugni et al. (2010), the pressure oscillation is divided into three regimes: The first peak (Regime A), the damped oscillation (Regime B), and small amplitude fluctuation (Regime C). Similarly, the pressure oscillation in the present experiment is categorized in three regimes: the first peak (Regime I, first period), the damped oscillation (Regime II, the subsequent four periods), and small amplitude fluctuation (Regime III, after five periods). In Regime I, the peak pressure is induced by the closure of the air cavity, which causes very large acceleration of water to the front wall. The second regime (Regime II) is the damped oscillation, in which the amplitude is strongly related to the wave front evolution. Thus, the air cavity evolution influences the pressure amplitude as the wave front evolution is affected by the air cavity evolution. In Fig. 7, the oscillation is not strictly damped that the trough shifts downward at the fourth period both for the waves of S1 and S2. For Fig. 7(a), the oscillation continues to be damped after the fourth period while the troughs of fourth and fifth period in Fig. 7(b) are still shifting downward. The remaining part (Regime III) governed by the gravity on the water volume along the front wall, resulting in very small amplitude fluctuation.

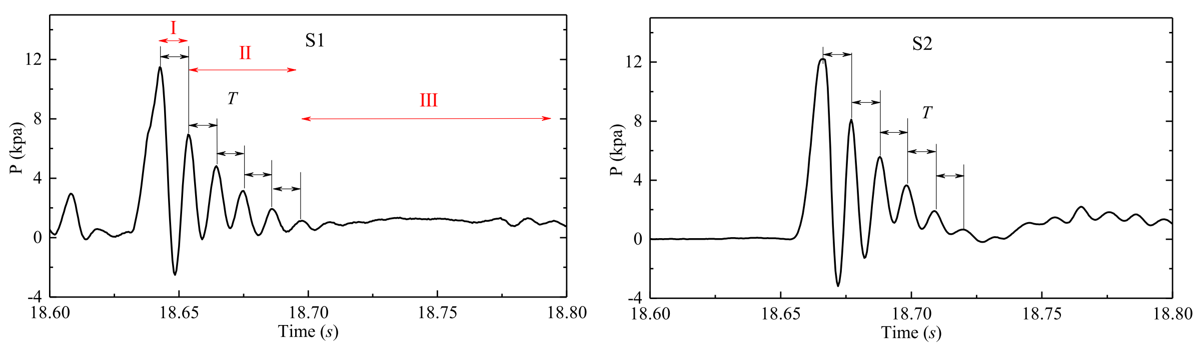

(a) (b)

Figure 7: Detail of pressure oscillation at FP2 of the wave of S1 and S2: (a) S1; (b) S2.

To elucidate the mechanism of air cavity evolution, the snapshots of air cavity for five periods in Regime I and II are listed in Fig. 8. The shape of air cavity is marked by the red line. In S1, the air cavity appears around two corners of the front wall while the air cavity just surrounds the upper corner of the front wall

Table 3: Maximal pressure on the front wall..

S1	Area of air cavity (cm^2)	Amplitude (kpa)	S2	Area of air cavity	Amplitude (kpa)
1T	78	11.552	1T	72	12.259
2T	51	7.011	2T	49	8.089
3T	43	4.835	3T	40	5.568
3T	58	3.098	4T	43	3.687
3T	54	2.035	5T	51	1.946

for the S2 case. The area of air cavity of S1 is larger than that of S2. In the first three periods for both S1 and S2 cases, the air cavity becomes smaller that the air escapes through the wave front. From the fourth period, the air cavity is inflated. Generally, the air inflation would result in the enlarged negative pressure value.

As indicated by Lugni et al. (2010), the pressure amplitude is highly dependent on the wave front evolution. It also means that the air cavity influences the pressure amplitudes because of the close relationship between the wave front evolution and air cavity. Thus, the area of air cavity is tracked to evaluate the pressure amplitudes. Orthogonal grids of uniform spacing are attached to the high-resolution images of wave snapshot to roughly estimate the area of air entrapment zone, as shown in Fig. 9. As the boundary (red line) of the air cavity is figured out, the area enclosed can be computed by counting the number of air cavity.

The area of air cavity and the amplitude of peak pressure for the cases of S1 and S2 are presented in Table 3. The amplitudes decrease monotonically while the area of air cavity decreases first and increases at last two periods. It is recalled that the phenomena in Fig. 7, Fig. 7(a) just shows one enlarged trough while Fig. 7(b) reveals two enlarged troughs. The reason may be the inflation of the air cavity, as indicated in Table 3. The air cavity of S1 becomes larger from 43 to 58 cm^2 and reduces to 54 cm^2. The air cavity of S2 continues to increase from 40 to 43 and 51. That is why S1 experienced one trough shifting downward while there are two troughs shifting downward in S2. If the value in Table 3 is normalized by maximal value in each column, the normalized scatter spots can be plotted in Fig. 10. In the first three periods, both the pressure amplitude and area of air cavity decrease. After the third period, the area of air cavity is inflating while the damped pressure amplitude is decreasing.

2.5. Repeatability test

Several studies have reported the variability of wave impact pressure in different repeats of the same case (Chan and Melville, 1988; Chan, 1994). The variations are mainly attributed to the experimental errors (e.g. real paddle motion and the initial condition of the fluid domain) and the randomness in the breaking-wave kinematics. To check the repeatability of the present experiment. S2 was repeated for three times. Before each test, the water in the wave flume is stationary so as to minimize the error from this factor. Because of those operations, the experimental errors in this repeat test are negligible. The pressure time histories of

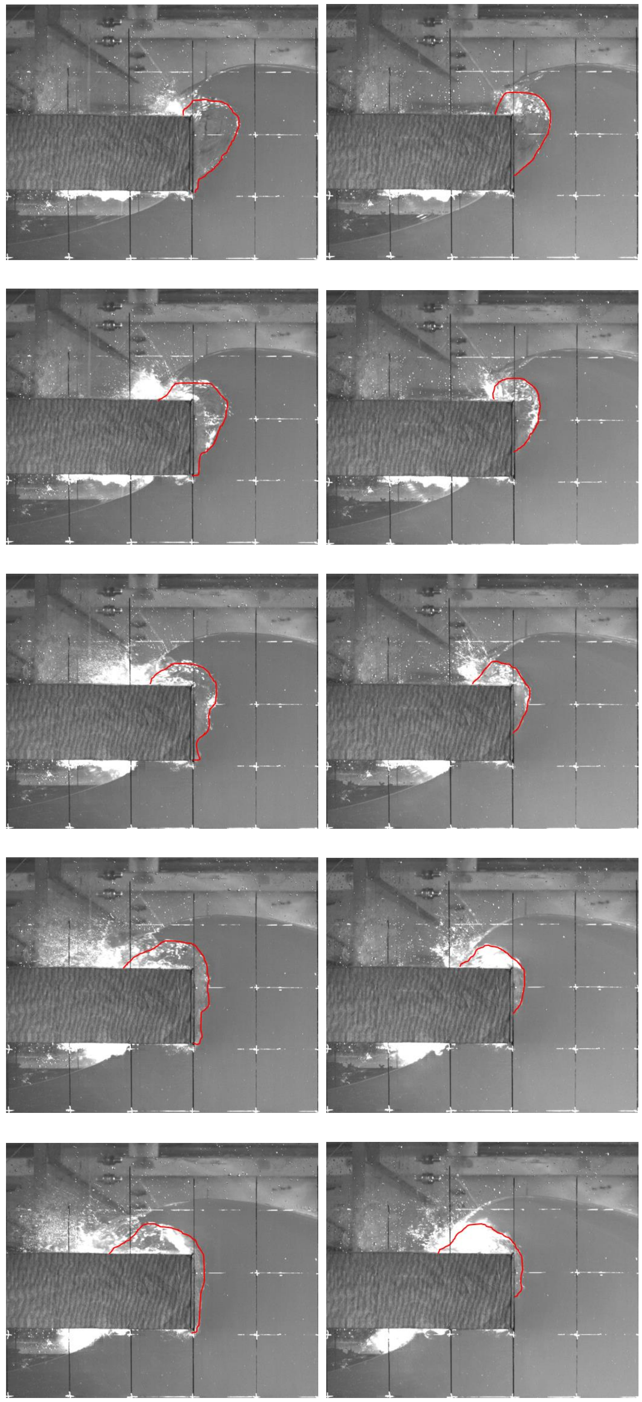

Figure 8: Snapshots of the air cavity evolution for two tests of S1 and S2. Left column: S1; Right Column: S2. The red solid line encloses the air cavity.

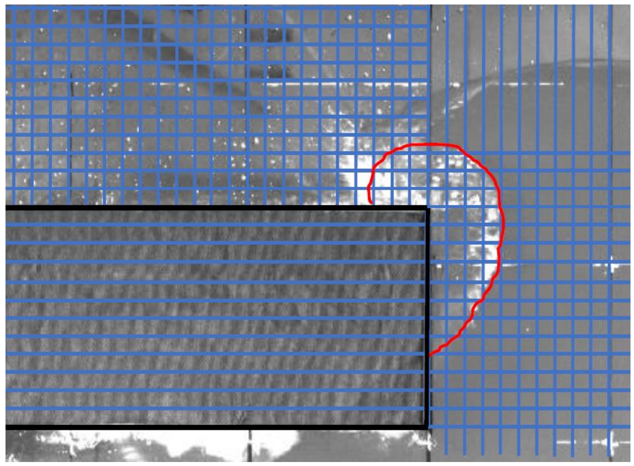

Figure 9: Sketch of the orthogonal grids attached to the wave snapshot to roughly estimate the area of air cavity. The solid black line stands for the shape of deck; The red line encloses the shape of air cavity.

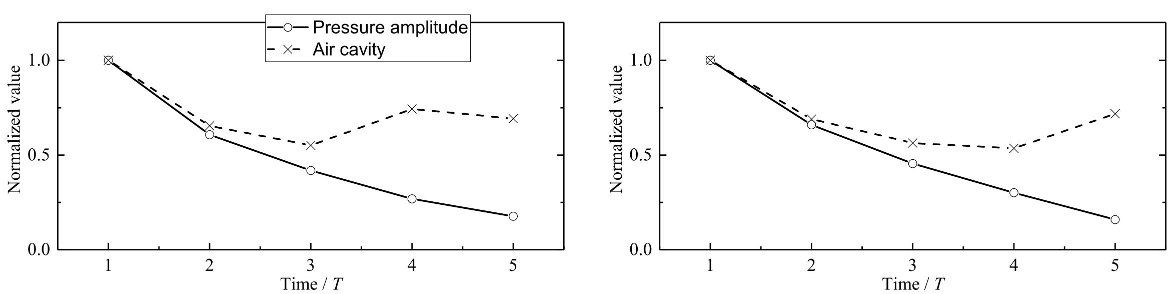

(a)

(b)

Figure 10: The relation between the pressure amplitude and area of air cavity.

three repeats are shown in Fig.11. The maximum variance in the whole time series is Fig.11(b), which is quite small. From Fig. 11, it can be seen that the pressure histories at the four measurement locations have almost the same general features and peak values although some minor differences exist. This is different from Chan and Melville (1988) and Chan (1994) who reported that the maximal pressure can vary by more than 100%. If the pressure variability does exist, one possible reason is that the measuring diaphragm (a circle of diameter 18mm) of the pressure sensor used in this study measures the average pressure of a finite area and hence the randomness in the extreme wave impact is filtered out. To reveal the detailed physics of this phenomenon, future researches are needed.

The repeatability can be further supported by the wave shape, as shown in Fig.12. The figure lists out the wave shapes for three tests when the wave is impacting the deck. The snapshots in each column present very similar wave shape, especially the wave front and the air entrained. In other words, the wave shape shows less variability for three repeating tests.

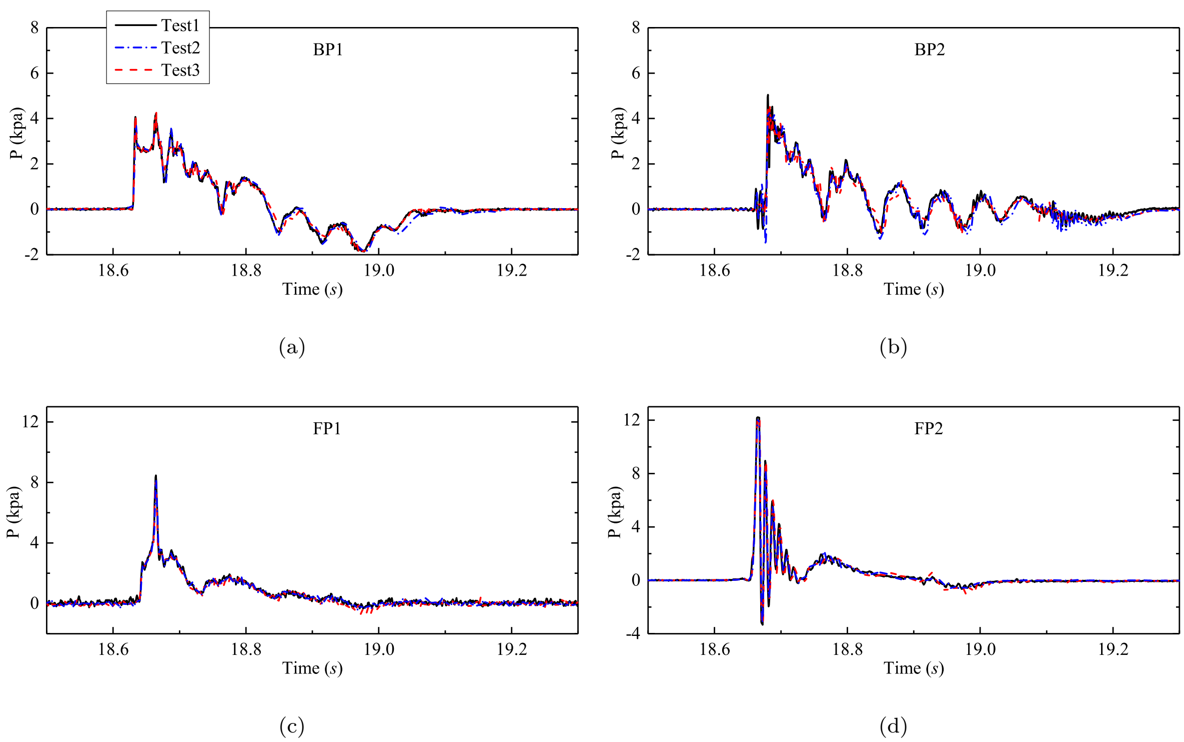

Figure 11: Repeatability test of pressure evolution at four gauges under the signal S2. Three test are presented.

3. Numerical simulation

In the numerical simulation, a Navier-Stokers solver combining with a level set method (Archer and Bai, 2015) is adopted to simulate the two-phase flow. The structure is modeled by an improved immersed boundary method from Yan et al. (2018). The detail is as follows.

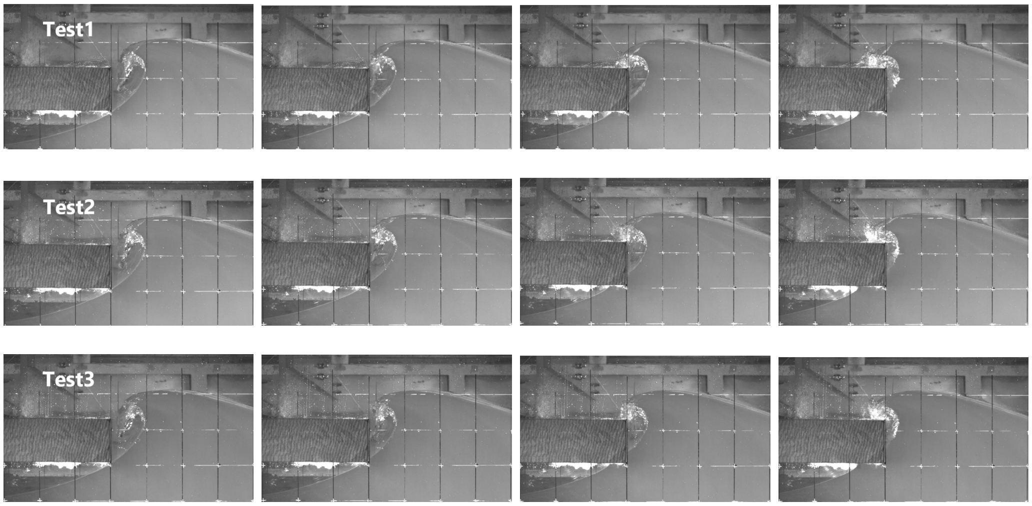

Figure 12: Snapshots of the wave impact process for three tests of S2. First row: Test1; middle row: Test2; third row: Test3.

3.1. Two-phase flow solver

For the 2D incompressible viscous fluid motion, the Navier-Stokes equations are used as the governing equations, including the momentum equations,

$$\frac{\partial u_i}{\partial t} + u_j \frac{\partial u_i}{\partial x_j} = \frac{1}{\rho}\left(-\frac{\partial p}{\partial x_i} + \frac{\partial \tau_{ij}}{\partial x_j}\right) + g_i + f_i, \tag{2}$$

and the continuity equation,

$$\frac{\partial u_i}{\partial x_i} = 0, \tag{3}$$

where u_i is the fluid motion velocity, located at the cell center face in a staggered grid system, x_i the orthogonal coordinate in space, t the time. For the variables at the cell center, p is the pressure, g_i the acceleration of gravity, ρ the fluid density, τ_{ij} the viscous stress components with the use of the Cartesian notation. Besides, f_i is the momentum added around an immersed boundary interface to model the structures.

A finite difference method is utilized to discretize the Navier-Stokes equations. The above variables are updated by a fractional step method (Archer and Bai, 2015). More details about discretizations are shown in Archer and Bai (2015) and Yan et al. (2018).

To capture the complicated wave surface, the level set method is adopted with the definition of a scalar distance function ϕ, which is to measure the shortest distance from the grid cell center to the interface. The distance function ϕ satisfies a convective equation,

$$\frac{\partial \phi}{\partial t} + u_i \frac{\partial \phi}{\partial x_i} = 0. \tag{4}$$

In the convective equation, the term $\frac{\partial \phi}{\partial x_i}$ is treated numerically by the fifth-order HJ-WENO scheme (Jiang and Peng, 2000). To continue, the value of ϕ at the next time-step can be updated by a third-order RK-TVD scheme, as indicated by Archer and Bai (2015).

3.2. Immersed boundary treatment

For the fluid-structure interaction, the solid phase is realized by adding a momentum forcing term near the boundary. The position of velocity vector that adds the forcing momentum term is defined as the forcing point. As the velocity vector is based on the staggered grid system, the boundary can not always coincide with the forcing points. Thus, the momentum forcing term should be calculated at the forcing points rather than enforced directly. Firstly, the forcing points ought to be located. To present a brief procedure for the forcing point search, Fig. 13 shows a sketch for illustration. In the figure, the line segment x_1-x_2 indicates the boundary and the solid phase is represented by the shadowed area. The procedure for locating forcing points can be seen in Yan et al. (2018), where the clear details were given.

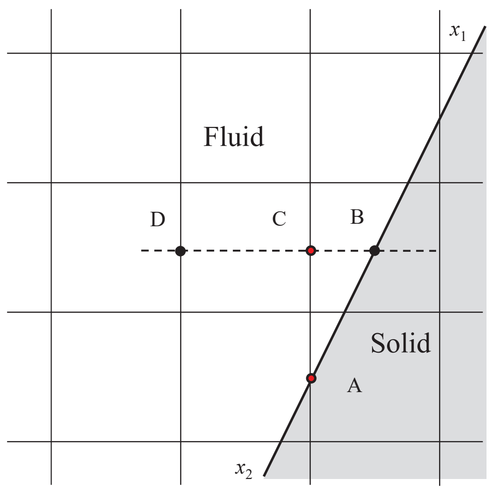

Figure 13: Illustration of the location and determination of imposed forcing component.

Since the forcing point is known, the predicted forcing component at the forcing point is based on the formula described in Mohd-Yusof (1997). The forcing term can be simply predicted by the following formula,

$$f_i = \frac{u_f - u_i^{n-1}}{\Delta t} - RHS_i^{n-1}. \tag{5}$$

where RHS is a sum of the convective, viscous, pressure gradient and body force terms in Eq. 2, the superscript n-1 denotes the value at the previous time step, and u_f is the velocity at the forcing point. If the forcing point is on the solid boundary, such as Point A in Fig. 13, $u_f = u_A$. Otherwise, u_f has to be calculated via the interpolation procedure from the surrounding flow field. Thus, the value of u_f can be interpolated via the velocities at Points B and D. Finally, the enforced momentum forcing term f_i is obtained.

3.3. Comparison of experimental and numerical results

The numerical model is validated against the experimental data. In the numerical simulations, in the region between the wave maker and the rear of the platform, the uniform mesh sizes along the horizontal and vertical directions are chosen to be 0.01 m and 0.005 m, respectively. In the rest area, the grid intervals of 0.02 m and 0.01 m in the horizontal and vertical directions are adopted. These grids ensure that the wave free surface can be captured and the structure can be modeled with good accuracy. For all three cases, the simulation of process of 20 s takes about 24 hours on a desktop PC with the CPU of Intel(R) Core i7-6700. As shown in Fig. 14, the wave elevations at WG1 and WG3 predicted by the present numerical model are in generally good agreement with the experimental measurements except that the wave crests and troughs are slightly underestimated with the difference about 4.1% and 2.8% at WG1 and WG3 respectively. Such small difference is probably due to the error of input signal. In the numerical simulation, the wave is generated by the velocity signal of wave paddle, while the experiment provides the displacement signal of wave paddle. The transformation from the displacement signal to velocity signal is carried out by the numerical differentiation over time where the error may occur. From the cases of S1 and S2, a minor difference between inputted signals could lead to the significant difference in wave elevations and pressures, as indicated in Figs. 4 and 5.

Fig. 15 shows the comparison of pressure time history between the experimental and numerical data. The trend of experimental pressure is captured well by the numerical model and the pressure magnitude at all four stations are underestimated. For the pressure at FP2, the impulse value is captured better than those at other three stations. Although the differences between the numerical and experimental wave elevations are generally small in Fig. 14, they may continue to grow just in front of the platform, which will cause a relatively larger discrepancy in wave impact pressures. In addition, the resolution of measurement equipment for wave elevation and pressure is also different. Finer mesh sizes have been tried, but the numerical results are very similar to the present ones. The pressure oscillation in the experiment is not reproduced (see Fig. 15(j) and Fig. 15(k)), because the air compressibility is not considered in the numerical model. In general, the developed numerical model is able to capture the key features of the wave elevation and impact pressure during a plunging wave impact process. Using the validated model, more detailed investigations on the wave impact pressure on the platform are conducted, as elaborated in the following two subsections.

3.4. Pressure distribution on the structure

It is costly and sometimes practically impossible to do a fine-resolution measurement of the pressure distribution on a structure. In contrast, such work can be done easily once a reliable numerical model is developed. Based on the validated numerical model, the pressure distributions at typical time instants on the front and bottom walls in the three cases are studied as shown in Fig. 16 and Fig. 17.

Firstly, the pressure distributions along the vertical front wall under the three wave scenarios are presented in Fig. 16. Fig. 16(a) captures a peak value 10.21 kpa around $y = 0.832$ m on the front wall in S1, which is close to the instant $t = 18.64$ s shown in the sub-figure of Fig. 4. The water jet licks the front wall with a

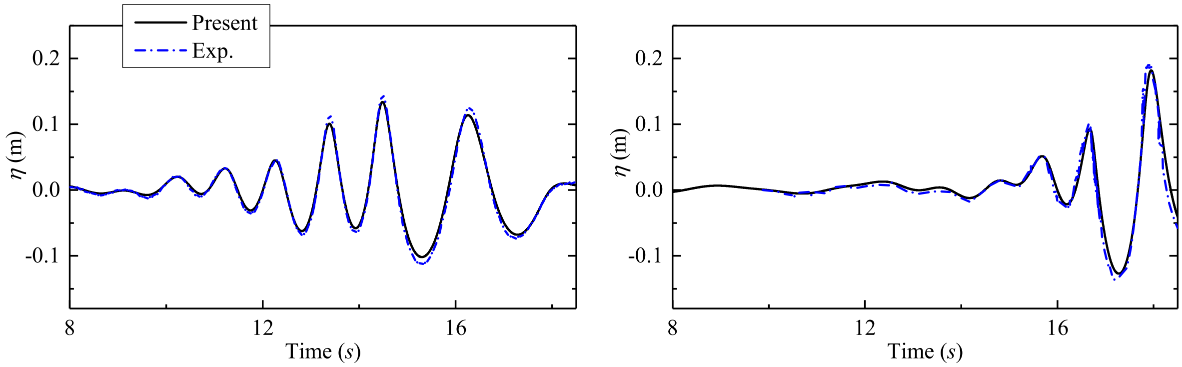

(a) (b)

Figure 14: Comparison between the experimental and numerical wave elevations with for signal S2: (a) WG1; (b) WG3.

large cavity surrounding the front wall, resulting in the largest pressure value. The wave of S2 impacts the front wall slightly later than that at S1 but the pressure distribution along the front wall is slightly different compared with Fig. 16(a). Fig. 16(b) captures a high peak value of 9.01 kpa, close to the instant $t = 18.66$ s Fig. 4. The Shape of Fig.16(b) is more like a pinnacle with a broader band than that in Fig. 16(a). In S3, the wave is not breaking yet when impacting on the platform (close to the instant $t = 18.70$ s Fig. 4), which leads to a distinguished wave impact pressure pattern, as shown in Fig.16(c). It is no longer an impulse in Fig. 16(a) or a pinnacle in Fig. 16(b). The maximal pressure value is located at $t = 18.7$ s, $y = 0.859$ m. As the bottom end of the front wall is still subjected to the propagating wave impact, the pressure value remains about 2.0 kpa at $y = 0.75$ m in Fig. 16(b) and Fig. 16(c).

The pressure distributions along the bottom wall under the three wave scenarios are presented in Fig. 17. For all 9 subfigures, with the distance far from the front wall (the upstream end of the bottom wall), the pressure begins to increase, reaching a maximum at a certain position, and reduces sharply to zero. The reason is that the whole bottom of the deck is not fully soaked. The part of the bottom wall contacting water is subjected to the larger pressure impact while the part contacting air bears very small pressure (almost zero). The pressure approaches the maximum at the demarcation point between the water and air on the bottom wall. The maximal pressure (3.47 kpa) on the bottom wall of S1 occurs at $t = 18.7$ s, $x = 13.80$ m in Fig. 17(b). For the S2 wave scenario, the maximal pressure value (approximately 3.38 kpa) occurs in Fig. 17(d) at one end rather than in the middle of the bottom wall. As the corner connected to the front and bottom wall is still subjected to the wave impact in S2, a very high pressure is captured in the upstream end of bottom wall. But in Fig. 17(d), a peak pressure is captured at $t = 18.7$ s with the magnitude of 3.17 kpa. In S3, The maximal pressure 3.16 kpa occurs at $t = 18.75$ s, $x = 14.12$ m. Those maximal pressures will be discussed in Fig. 18.

The spatial and temporal distribution of peak pressures on the front and bottom walls of the three cases

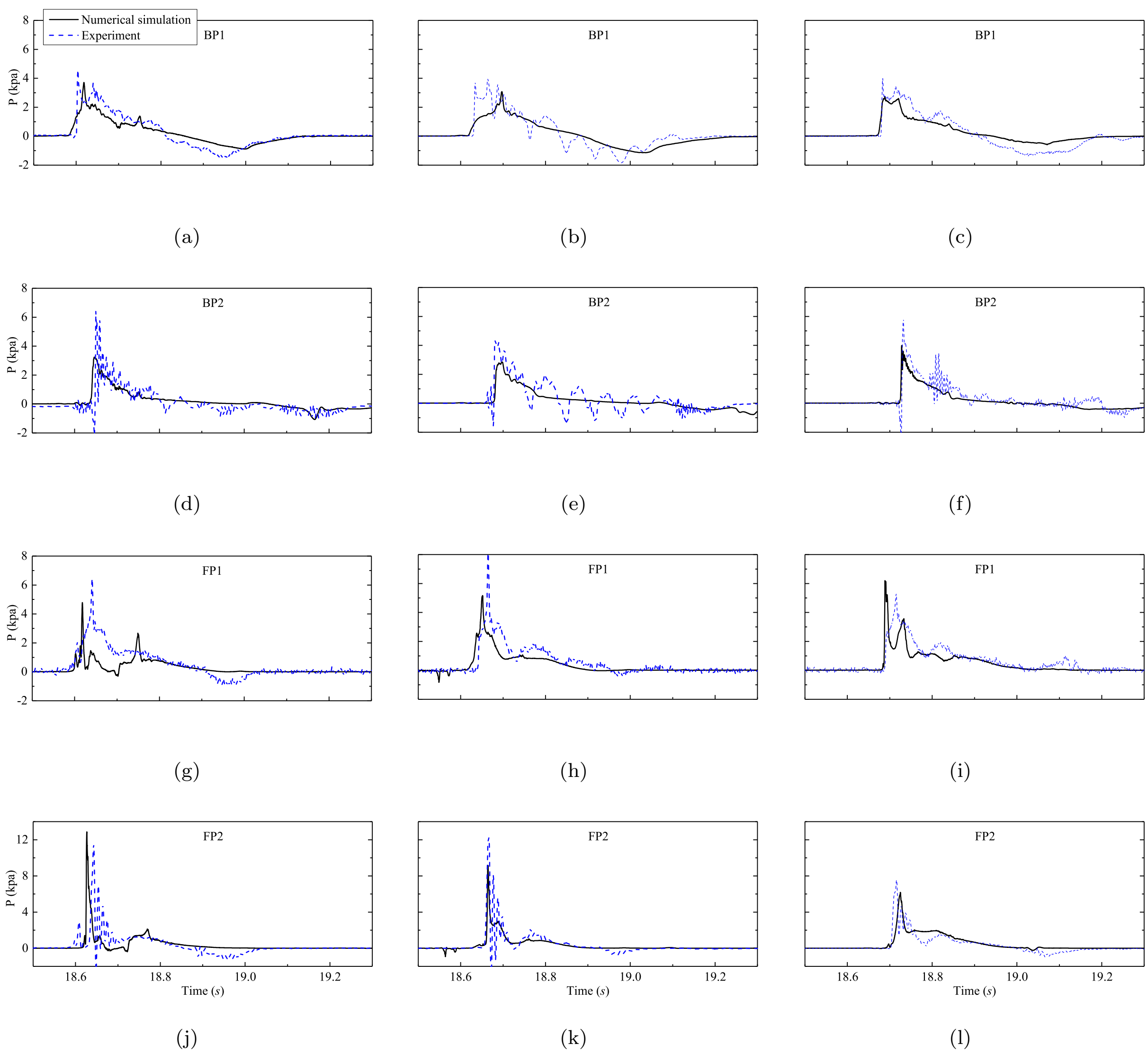

Figure 15: Comparison of impact pressures on the front (FP1 & FP2) and bottom (BP1 & BP2) walls of the platform for the 3 wave scenarios (left: S1; middle: S2; right: S3).

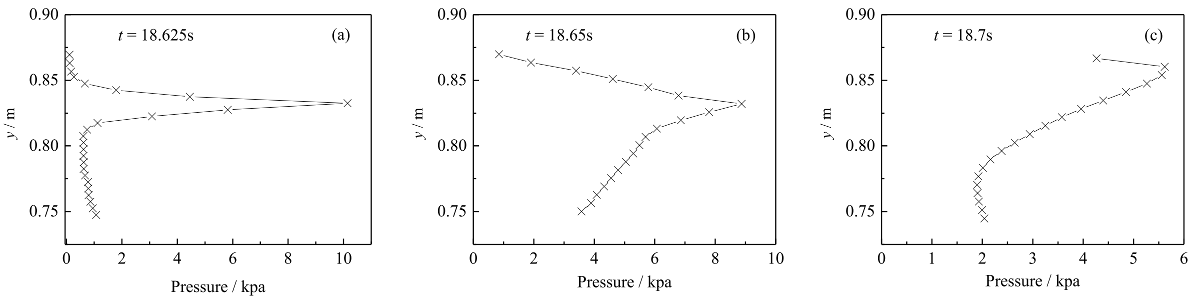

(a) S1 (b) S2 (c) S3

Figure 16: Pressure distributions along vertical front wall under the three wave scenarios: (a) S1. (b) S2; (c[]) S3.

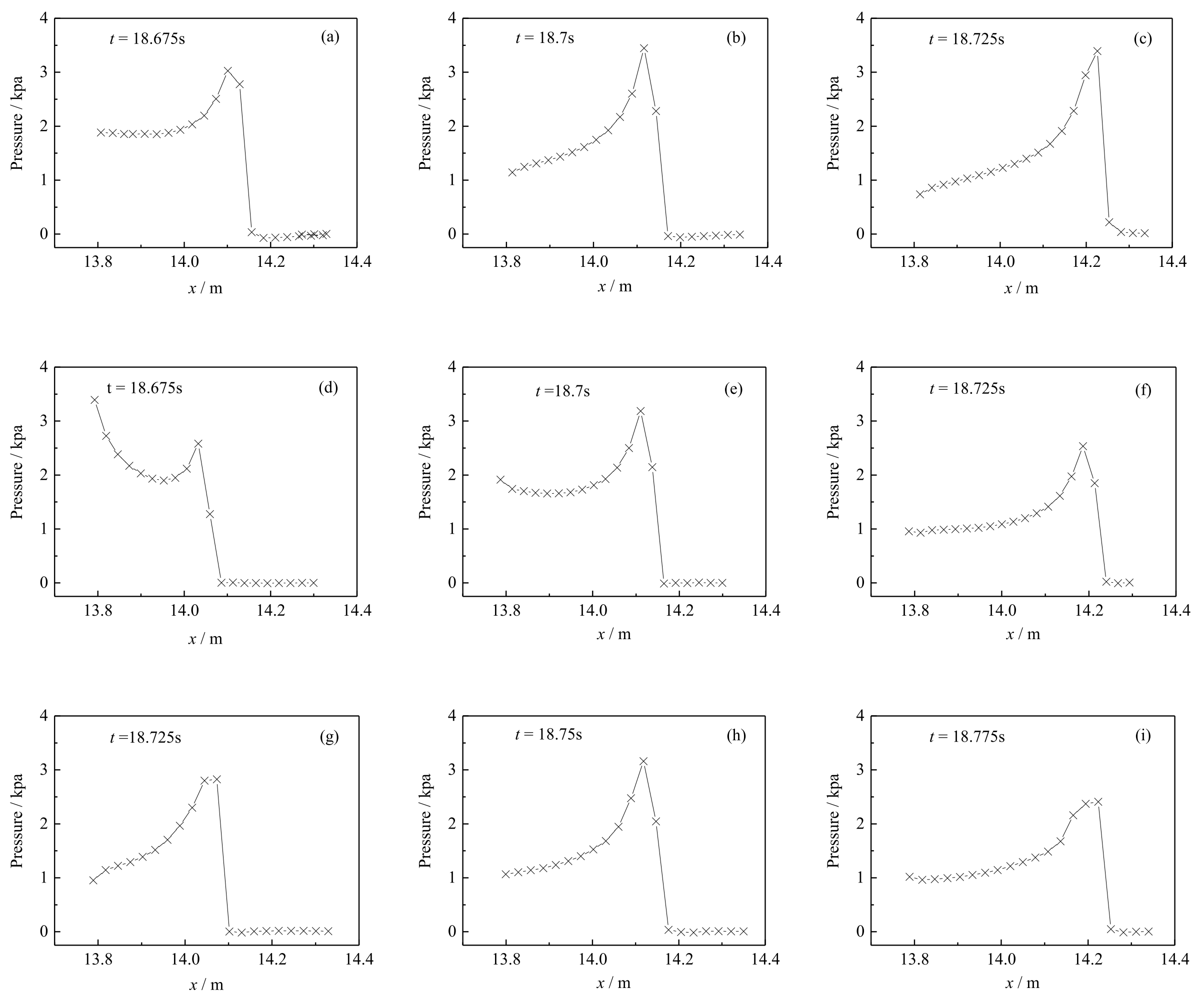

Figure 17: Pressure distributions along the horizontal bottom wall. Up row: S1; middle row: S2; bottom row: S3.

are presented in Fig. 18. In Fig. 18(a), the time interval of maximal pressure between S2 and S3 is almost two times of that between S1 and S2. The peak pressure bearing point moves upwards along the front wall from S1 to S3. Fig. 18(b) collects the maximal pressure points along the bottom wall. The maximal values for S1 and S2 occur at the very close position (x = 14.12 m). However, for S2, a special case happens that the maximal value occurs at one end of the bottom wall, rather than at the position around x = 14.11 m. At x = 14.11 m, S2 can still capture a peak value of 3.17 kpa, smaller than 3.38 kpa. The overall sequence of maximal pressure is S1 > S2 > S3.

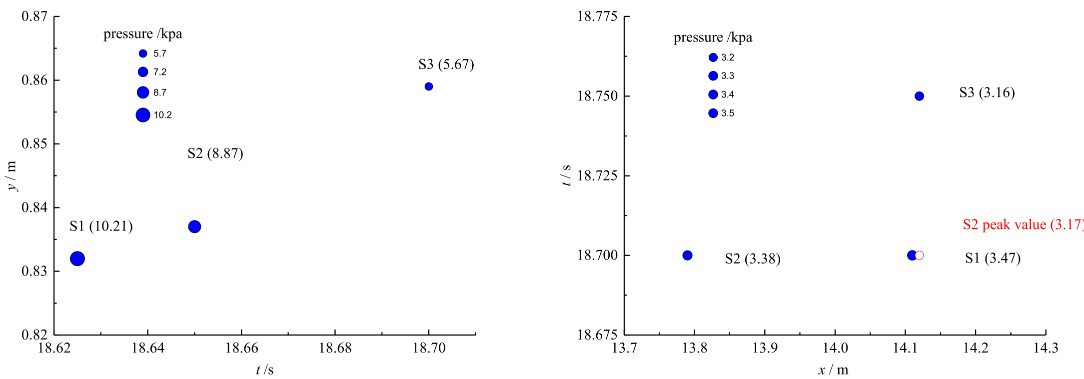

(a) (b)

Figure 18: Spatial and temporal distribution of maximal pressure: (a) along the front wall; (b) along the bottom wall.

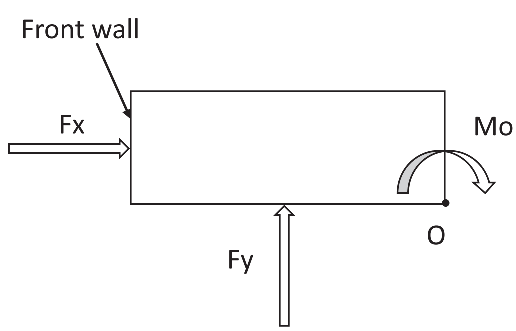

Figure 19: Sketch of force and moment directions on the platform.

In addition, the horizontal and vertical forces and moment (calculated on the rear of platform deck) on the platform are evaluated by integrating the wave impact pressure on the whole platform, which are presented in Fig. 20. To be clearly, the directions of force and moment on the platform are indicated in Fig. 19. These three sub-figures show the similar feature to the time histories of impact pressure. The time intervals of peak value among different wave impacts are the same indicated in Fig. 5. The only difference is that the wave impact S3 imposes the largest force and moment on the deck, as the area subjected to impact is larger. As the wave of S2 leads to the smaller impact pressure, an integration of impact pressure over the whole contact area is a little bit smaller. It is also observed that the loads of S3 are larger than those of S1 and S2 (entrained more air). The magnitude of the force or moment is S3 > S1 > S2.

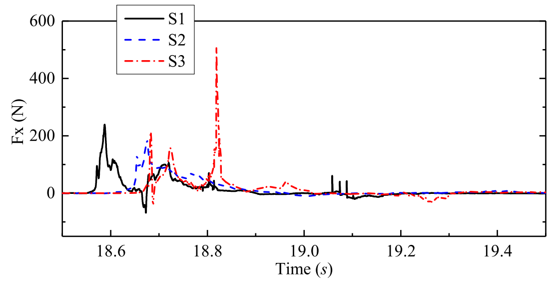

(a) Horizontal foce

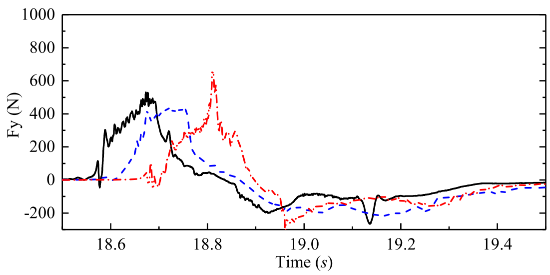

(b) Vertical force

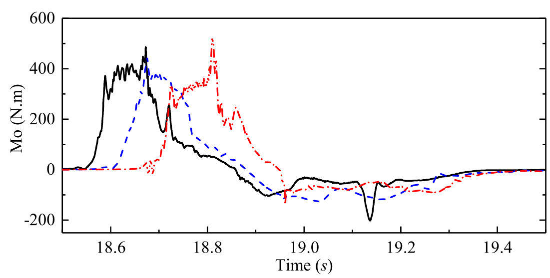

(c) Moment

Figure 20: Horizontal, vertical force, and moment on the deck.

3.5. Pressure maximum

For the purpose of practical application, it is important to analyze the wave impact pressure or force as a dimensionless parameter. Two significant studies are Blackmore and Hewson (1984) and Cuomo et al. (2010). The peak pressures on the front wall of the box-shape structure in the present study are normalized by the approaches in these two studies, and compared with the documented peak pressure ranges, as presented in Table 4. The normalized pressure of S1 and S2 is larger than that of S1. And the wave scenarios S1 and S2 entrain the air while there is little air entrapped in S3. It reveals that the air presence enlarges the impact

Table 4: Normalized pressure maximum on the front wall for different normalization approaches.

Types	$p_{max}/\rho C^2 T$			$p_{max}/\rho g H_D$	
	Present	Chan (1994)	Blackmore and Hewson (1984)	Present	Cuomo et al. (2010)
S1	1.86			3.89	
S2	1.77	8.8∼18.5	1∼10	3.70	1.0∼4.5
S3	1.06			2.22	

pressure, consistent with the conclusions in Wood Deborah et al. (2000) and Bredmose et al. (2015). It also finds that the maximal pressures on a fixed box structure under the plunging wave circumstances of this study are located in the observed pressure ranges by Blackmore and Hewson (1984) and Cuomo et al. (2010). The normalized pressure from Chan (1994) deviates much from the range 1∼10. It also reflects the bad repeatability of experiments, stated in Subsection 2.4. Conducting more work so as to figure out a more accurate peak pressure range for the box-shape structure is of great significance, which will be the future work.

4. Conclusions

The paper investigates the plunging wave impacts on a box-shape structure experimentally and numerically. Three impact scenarios are studied, i.e. impact after wave breaking (S1), impact upon wave breaking (S2), and impact before wave breaking (S3). Both experimental and numerical results show that the impacts of S1 and S2 possess the similar pressure magnitudes. The front wall bears the larger impact pressure than the bottom wall. The pressure oscillation is observed on the front wall that it is strongly correlated with the evolution of air cavity by examining the area of air cavity. The existence of air cavity results in the larger maximal positive and negative pressure. The amplified pressure easily causes the local damages to the designed structure. In addition, the repeatability test of S2 are carried out for three times that the pressure time histories repeat well. The numerical results from an improved immersed boundary method is compared with the experiment. A roughly good agreement is obtained for the wave elevations. The numerical method captures the key features of impact pressures. The numerical pressure distributions reflect that the pressure distributions on the front wall under three wave scenarios follow different modes. However, it is very similar for the pressure distributions on the bottom wall under the three wave scenarios.

Finally, two normalizations for pressure maximum are presented that the present normalized pressure maximums are located in the corresponding range of Blackmore and Hewson (1984) and Cuomo et al. (2010). However, the normalized pressure maximum from Chan (1994) is much larger than the present result. It also deviates much from the range of $1 \sim 10$. By the comparison of the maximal impact pressures among three wave scenarios, the presence of aeration indeed increases the impact pressure maximum.

References

Abdussamie, N., Ojeda, R., Thomas, G. and Amin, W. (2016). Measurements of global and local effects of wave impact on a fixed platform deck, *Proceedings of the Institution of Mechanical Engineers, Part M: Journal of Engineering for the Maritime Environment* **231**(1): 212–233.

Abrahamsen, B. C. and Faltinsen, O. M. (2012). The natural frequency of the pressure oscillations inside a water-wave entrapped air pocket on a rigid wall, *Journal of Fluids and Structures* **35**: 200–212.

Archer, P. and Bai, W. (2015). A new non-overlapping concept to improve the hybrid particle level set method in multi-phase fluid flows, *Journal of Computational Physics* **282**: 317–333.

Biesel, F. and Suquet, F. (1951). Les apparails generateurs de houle en laboratoire, *La Houille Blanche* **6**: 4.

Blackmore, P. A. and Hewson, P. J. (1984). Experiments on full-scale wave impact pressures, *Coastal Engineering* **8**(4): 331–346.

Bredmose, H., Bullock, G. N. and Hogg, A. J. (2015). Violent breaking wave impacts. Part 3. effects of scale and aeration, *Journal of Fluid Mechanics* **765**: 82–113.

Bredmose, H., Hunt Raby, A., Jayaratne, R. and Bullock, G. N. (2010). The ideal flip-through impact: experimental and numerical investigation, *Journal of Engineering Mathematics* **67**(1): 115–136.

Bullock, G. N., Obhrai, C., Peregrine, D. H. and Bredmose, H. (2007). Violent breaking wave impacts. Part 1: Results from large-scale regular wave tests on vertical and sloping walls, *Coastal Engineering* **54**(8): 602–617.

Chan, E. S. (1994). Mechanics of deep water plunging-wave impacts on vertical structures, *Coastal Engineering* **22**(1): 115–133.

Chan, E. S. and Melville, W. K. (1988). Deep-water plunging wave pressures on a vertical plane wall, *Proceedings of the Royal Society of London A: Mathematical, Physical and Engineering Sciences*, Vol. 417, pp. 95–131.

Cuomo, G., Allsop, W., Bruce, T. and Pearson, J. (2010). Breaking wave loads at vertical seawalls and breakwaters, *Coastal Engineering* **57**(4): 424–439.

Faltinsen, O. M., Landrini, M. and Greco, M. (2004). Slamming in marine applications, *Journal of Engineering Mathematics* **48**(3): 187–217.

Gao, R., Ren, B., Wang, G. and Wang, Y. (2012). Numerical modelling of regular wave slamming on subface of open-piled structures with the corrected sph method, *Applied Ocean Research* **34**: 173–186.

Guilcher, P.-M., Couty, N., Brosset, L. and Le Touz, D. (2013). Simulations of breaking wave impacts on a rigid wall at two different scales with a two-phase fluid compressible sph model, *International Journal of Offshore and Polar Engineering* **23**(4): 182–190.

Hu, Z. Z., Mai, T., Greaves, D. and Raby, A. (2017). Investigations of offshore breaking wave impacts on a large offshore structure, *Journal of Fluids and Structures* **75**: 99–116.

Jiang, G. and Peng, D. (2000). Weighted ENO schemes for Hamilton-Jacobi equations, *SIAM Journal on Scientific Computing* **21**(6): 2126– 2143.

Lind, S. J., Stansby, P. K., Rogers, B. D. and Lloyd, P. M. (2015). Numerical predictions of waterair wave slam using incompressiblecompressible smoothed particle hydrodynamics, *Applied Ocean Research* **49**: 57–71.

Lugni, C., Brocchini, M. and Faltinsen, O. M. (2010). Evolution of the air cavity during a depressurized wave impact. ii. the dynamic field, *Physics of Fluids* **22**(5): 056102.

Luo, M., Koh, C. G., Bai, W. and Gao, M. (2016). A particle method for two-phase flows with compressible air pocket, *International Journal for Numerical Methods in Engineering* **108**(7): 695–721.

Ma, Y., Dong, G., Perlin, M., Liu, S., Zang, J. and Sun, Y. (2009). Higher-harmonic focused-wave forces on a vertical cylinder, *Ocean Engineering* **36**(8): 595–604.

Mohd-Yusof, J. (1997). Combined immersed boundary/B-spline method for simulations of flows in complex geometries, *Technical report*, Center Annual Research Briefs, NASA Ames/Stanford University.

Qin, H., Tang, W., Xue, H. and Hu, Z. (2017). Numerical study of nonlinear freak wave impact underneath a fixed horizontal deck in 2-d space, *Applied Ocean Research* **64**: 155–168.

Ren, B., Li, X. L. and Wang, Y. X. (2006). Experimental investigation of instantaneous properties of the flow field of wave slamming, *Ocean Engineering* **24**(4): 68–74.

Topliss, M., Cooker, M. and Peregrine, D. (1993). Pressure oscillations during wave impact on vertical walls, *23rd International Conference on Coastal Engineering*.

Wood Deborah, J., Peregrine, D. H. and Bruce, T. (2000). Wave impact on a wall using pressure-impulse theory. Part I: Trapped air, *Journal of Waterway, Port, Coastal, and Ocean Engineering* **126**(4): 182–190.

Yan, B., Bai, W. and Quek, S. T. (2018). An improved immersed boundary method with new forcing point searching scheme for simulation of bodies in free surface flows, *Communications in Computational Physics* **24**(3): 830–859.

Zhao, X. and Hu, C. (2012). Numerical and experimental study on a 2-D floating body under extreme wave conditions, *Applied Ocean Research* **35**: 1–13.